

Article

Fe_{1-x}S Modified TiO₂ NPs Embedded Carbon Nanofiber Composite via Electrospinning: A Potential Electrode Material for Supercapacitors

Bishweshwar Pant¹, Hem Raj Pant² and Mira Park^{1,*}

¹ Department of Biomedical Sciences and Institute for Medical Science, Jeonbuk National University Medical School, Chonbuk 54907, Korea; bisup@jbnu.ac.kr

² Department of Applied Sciences, Tribhuvan University, Kathmandu 44600, Nepal; hempant@ioe.edu.np

* Correspondence: wonderfulmira@jbnu.ac.kr

Academic Editor: Dipendu Saha

Received: 7 January 2020; Accepted: 26 February 2020; Published: 27 February 2020



Abstract: Fe_{1-x}S-TiO₂ nanoparticles embedded carbon nanofibers (Fe_{1-x}S-TiO₂/CNFs) composite as a supercapacitor electrode material has been reported in the present work. The Fe_{1-x}S-TiO₂/CNFs composite was fabricated by electrospinning technique followed by carbonization under argon atmosphere and characterized by the state-of-art techniques. The electrochemical studies were carried out in a 2 M KOH electrolyte solution. The synthesized material showed a specific capacitance value of 138 F/g at the current density of 1 A/g. Further, the capacitance retention was about 83%. The obtained results indicate that the Fe_{1-x}S-TiO₂/CNFs composite can be recognized as electrode material in supercapacitor.

Keywords: Fe_{1-x}S-TiO₂; carbon nanofibers; composite; electrospinning; energy storage

1. Introduction

Due to the ever-increasing energy demand, developing efficient and environmentally friendly energy storage devices has become one of the major tasks among the researchers. Supercapacitors have been recognized as a reliable and efficient energy storage device in recent years [1–3]; however, the performance of supercapacitors must be significantly improved to fulfill the future global energy demand. Since the electrochemical properties of electrode play an important role in the overall performance of supercapacitor, the fabrication of high-performance electrode material with an excellent electrochemical performance is essential [1,4].

Recently, transition metal oxides such as Co₃O₄, Fe₂O₃, RuO₂, NiO, ZnO, TiO₂, MgO, MnO₂ have been applied as electrode material for supercapacitors [1,3,5,6]. Among them, TiO₂ as one of the typical pseudocapacitance materials has attracted immense interest for supercapacitors due to its high stability, low-cost, excellent electrochemical stability, and nontoxicity [4,7,8]. However, one major issue is the poor electric conductivity that limits its power density and rate capability [9]. To overcome this problem, most of the reports have been focused on combining TiO₂ with conductive carbon materials such as carbon nanofibers [4], graphene [7], and carbon nanotubes [10]. The carbon nanofibers offer mechanical and physicochemical stability of the composite, as well as prevent the aggregation of metal oxide nanoparticles [3,11]. In addition, the carbon nanofibers possess high electrical conductivity, high charge transfer ability, large surface area and mesoporosity, and high electrolyte accessibility [12]. Therefore, integrating TiO₂ into the carbon structures shows the combined effect of the pseudocapacitance of metal oxide and double-layer capacitance of carbon. In our previous study [4], we fabricated TiO₂ NPs embedded carbon nanofibers via the electrospinning technique and applied as a supercapacitor electrode. It was observed that after incorporating TiO₂ into carbon fibers, the specific capacitance of the TiO₂ was enhanced by ~2.3 times [4].

Among transition metal compounds, metal sulfides have been identified as the alternative material for supercapacitor electrode [13,14]. As compared to their metal oxides counterparts, metal sulfides show better performance for practical application due to the smaller volume change and higher efficiency. In particular, Fe_{1-x}S nanostructures are emerging materials for supercapacitors and lithium-ion batteries due to their abundance in nature, cost-effectiveness, mechanical stability, and relatively large capacity compared with other metal sulfides [15–18]. However, low conductivity, sluggish kinetics, possible dissolution of sulfur, and severe volume change during the cyclic use are the issues of using iron sulfides in supercapacitor. Therefore, effective strategies should be developed to overcome these limitations for practical applications. One effective way to enhance the conductivity and buffer the volume expansion during the charge-discharge process is fabricating composite with conductive carbon materials especially, carbon nanofibers [18,19]. Taking all these factors into consideration, in this contribution, we prepared $\text{Fe}_{1-x}\text{S-TiO}_2$ decorated carbon nanofibers ($\text{Fe}_{1-x}\text{S/TiO}_2/\text{CNFs}$) by the electrospinning process followed by direct carbonization under an inert atmosphere of argon. The combination of $\text{Fe}_{1-x}\text{S-TiO}_2$ and conductive carbon nanofibers should be greatly beneficial to the structural ability and overall performance of the composite electrode. Such a novel structure exhibited enhanced electrochemical performance as compared to pristine TiO_2 nanofibers.

2. Experimental

2.1. Materials

Iron (III) acetylacetonate, ethanol, polyvinylpyrrolidone (PVP), acetic acid, titanium tetraisopropoxide (97%), ammonium sulfide solution (40–48 wt % in H_2O), and polyvinylidene fluoride (PVDF) were purchased from Sigma-Aldrich. *N*-methyl-2-pyrrolidone (NMP) (99.5%) was purchased from Showa Chemicals Inc., Tokyo, Japan. Potassium hydroxide (99.5%) was obtained from Samchun Pure Chemical Co. Ltd., Seoul, South Korea. All chemicals were of analytic grade and used without any purification.

2.2. Synthesis of $\text{Fe}_{1-x}\text{S-TiO}_2/\text{CNFs}$ Composite

Figure 1 depicts the synthetic protocol for the fabrication of $\text{Fe}_{1-x}\text{S-TiO}_2/\text{CNFs}$ composite. All the chemicals in this experiment were purchased from Sigma-Aldrich. In the beginning, 0.5 g of PVP and 5 g of ethanol were taken in a glass vial and stirred for 2 h. Next, 0.45 g of Iron (III) acetylacetonate was mixed to the solution followed by the addition of 0.3 mL of ammonium sulfide and stirred for 1 h. In a separate vial, 1.5 g of titanium tetraisopropoxide was added to 3 g of acetic acid. After 10 min of stirring, it was transferred to the aforementioned PVP solution and stirred for 3 h at room temperature to form a homogeneous mixture. The electrospinning technique (NanoNC electrospinning system) was applied to fabricate nanofibers membrane from the resulting precursor/polymer solution. During the electrospinning process, the tip-to-collector distance and applied voltage were 15 cm and 18 kV, respectively. A polyethylene sheet was wrapped around the collector for collecting the nanofiber mat. The collected nanofibers mat was vacuum dried at 60 °C for 12 h. After carbonization in the argon atmosphere at 850 °C for 3 h, the sample was used for further analyses. For comparison, we prepared TiO_2 NFs by following the same procedure as in our previous reports [4,20]. Briefly, the PVP solution containing titanium tetraisopropoxide was electrospun into the nanofiber under the identical conditions as mentioned above and the obtained nanofiber mat was subjected to calcination in air at 600 °C for 3 h to obtain TiO_2 NFs.

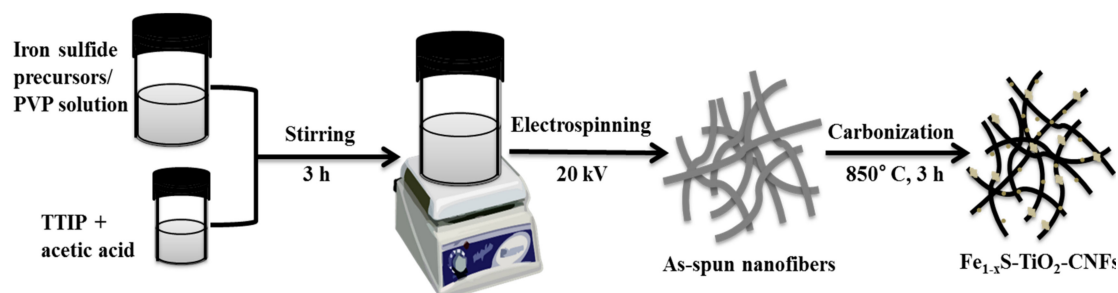


Figure 1. Schematic diagram showing the preparation of $\text{Fe}_{1-x}\text{S-TiO}_2$ nanoparticles embedded carbon nanofibers ($\text{Fe}_{1-x}\text{S-TiO}_2/\text{CNFs}$) composite.

2.3. Characterization

A morphological study of the sample was conducted by field emission scanning electron microscopy (FE-SEM, S-7400, Hitachi, Tokyo, Japan) and transmission electron microscopy (TEM, JEM-2010, JEOL, Tokyo, Japan). X-ray diffraction patterns (XRD) were collected at room temperature by using the X-ray diffractometer (Rigaku Co., Tokyo, Japan). The Fourier transform infrared (FTIR) spectra were recorded using an ABB Bomen MB100 spectrometer (Bomen, QC, Canada). The spectrum and origin were used to analyze and fit the FTIR spectra. The X-ray photoelectron spectroscopy (XPS) analyses were carried out by (XPS; Thermo Fisher Scientific, Loughborough, UK) and the data were fitted with origin. Brunauer–Emmett–Teller (BET) and Barrett–Joyner–Halenda (BJH) studies for the specific surface area and porosity of the sample were evaluated on an ASAP 2020 Plus system (Micromeritics Instrument Corp., Norcross, GA, USA).

2.4. Electrochemical Studies

The working electrodes were prepared by coating the nickel foam with a homogenous slurry of as-prepared samples, carbon black, and polyvinylidene fluoride (PVDF) at a weight ratio of 8:1:1 in *N*-methyl-2-pyrrolidone (NMP). The substrate was then dried at 60 °C overnight. The electrochemical performance was investigated with a conventional three-electrode electrochemical analyzer (VersaSTAT3, Algete-Madrid, Spain) at room temperature in a 2 M KOH solution as an electrolyte. Nickel foam, Ag/AgCl, and Pt wire were used as the working, reference, and counter electrodes, respectively. Cyclic voltammetry (CV), galvanostatic charge–discharge (GCD), electrochemical impedance spectroscopy (EIS), and the stability by charge–discharge cycles were performed using Versastate3. The CV tests were carried out at different scanning rates (10, 20, 30, 40, 50, 60, 70, 80, 90, and 100 mV/s) from 0.0 to 0.5 V. GCD tests were performed from 0 to 0.45 V at different current densities (1, 2, 3, 4, and 5 A/g). The EIS was measured from 100 kHz to 0.01 Hz. The specific capacitance of the electrodes was calculated by the GCD method by applying the equation below:

$$C = \frac{I \cdot \Delta t}{m \cdot \Delta V} \quad (1)$$

where ‘*C*’ is the specific capacitance (F/g), ‘*I*’ is the charge-discharge current (A), ‘*t*’ is the discharge time (s), ‘*m*’ is the mass of the active material (g), and ‘*V*’ is the potential window (V).

3. Results and Discussion

Figure 2A,B depicts the FE-SEM images of TiO_2 NFs and $\text{Fe}_{1-x}\text{S-TiO}_2$ -CNFs composite, respectively. The pristine TiO_2 NFs showed continuous and smooth morphology. It should be noted that the TiO_2 nanofibers were prepared from titanium tetraisopropoxide/PVP nanofibers by calcination at 600 °C for 3 h. During the calcination process, the PVP was selectively removed and continuous TiO_2 NFs were obtained. When the electrospun PVP nanofibers containing titanium tetraisopropoxide and iron sulfide precursors were directly carbonized under the argon atmosphere, the PVP was carbonized and

titanium tetraisopropoxide was decomposed to give TiO_2 NPs, thereby resulting in the formation of $\text{Fe}_{1-x}\text{S-TiO}_2$ incorporated carbon nanofibers (Figure 2B). Since the addition of sulfide ions in the iron precursor may result in the formation of iron chalcogenide, the nanofibers should have $\text{Fe}_{1-x}\text{S-TiO}_2$ particles embedded in the carbon matrix. It is noticeable that the nanofiber morphology was preserved even after the carbonization process. The TEM image in Figure 2C clearly shows the projection of particles from the body of carbon nanofiber. To confirm the successful loading of the iron sulfide- TiO_2 NPs in the carbon nanofibers, elemental mapping was carried out. As in Figure 2D, the mapping study detected C, Ti, O, Fe, and S, showing the presence of all elements present in the fiber synthesis.

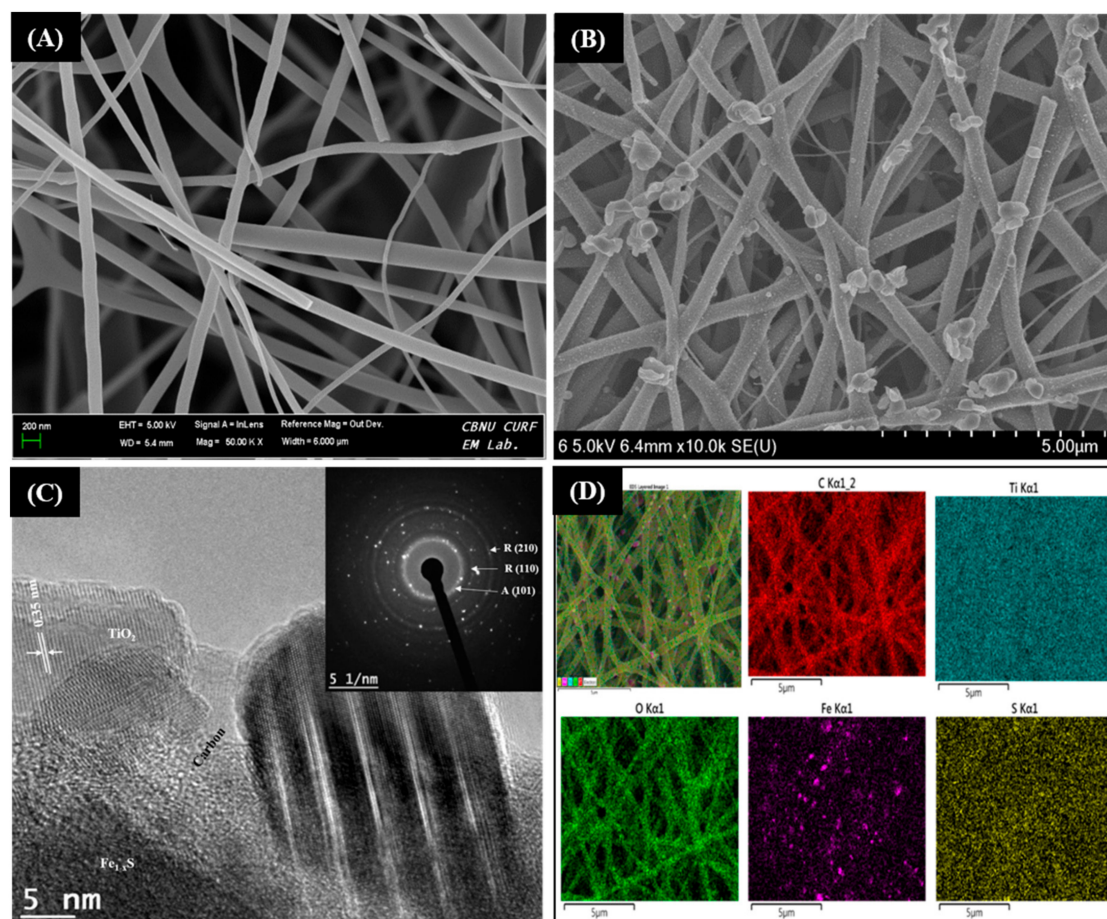


Figure 2. FE-SEM images of pristine TiO_2 NFs (A) and $\text{Fe}_{1-x}\text{S-TiO}_2/\text{CNFs}$ composite (B). (C) and (D) are the TEM image and elemental mapping of the $\text{Fe}_{1-x}\text{S-TiO}_2/\text{CNFs}$ composite, respectively. The inset of (C) represents the SAED pattern.

The phase structure and crystallinity of the as-obtained nanofibers were studied by XRD patterns, as shown in Figure 3A. The pristine TiO_2 nanofibers showed both anatase and rutile phase. The apparent peaks for anatase were observed at 2θ values of 25.1, 38, 47.89, and 75° which were corresponding to the (101), (004), (200), and (125) phase, respectively [20]. Similarly, the existence of crystalline peaks at 2θ values of 27.3, 36, 41.2, 54.25, 62.4, 68.73, and 70.1° corresponding with the crystal plane of (110), (101), (111), (211), (002), (301), and (112), respectively represent the rutile phase of TiO_2 NFs [20]. It should be noted that the anatase peaks are highly suppressed and the rutile peaks are dominant in the $\text{Fe}_{1-x}\text{S-TiO}_2/\text{CNFs}$ composite sample. Moreover, a strong peak appeared at 2θ values of 44.7° which corresponds to (210) crystal plane of rutile TiO_2 . Previous studies have also shown that the crystallinity of TiO_2 is affected by the temperature [4,21,22]. Since the synthesis of $\text{Fe}_{1-x}\text{S-TiO}_2/\text{CNFs}$ was carried out at higher temperature (850°C) as compared to TiO_2 NFs (600°C), the higher thermal treatment played a role in the transformation of the crystal phase from anatase to rutile [23]. In addition

to the rutile peaks, a small and broad peak between 2θ values of 22 and 23° was observed, which is attributed to the (002) plane of the amorphous carbon [23,24]. This finding indicated that the PVP was successfully converted into the carbon under inert atmosphere during the carbonization process. Additionally, the peaks at 2θ values of 30.3 and 43.6° corresponding to the (200) and (210) planes of Fe_{1-x}S were observed (JCPDS # 29-0724) [25,26]. The selected area electron diffraction (SAED) in the inset in Figure 2C also shows the polycrystalline nature of the prepared sample. The interaction between the Fe_{1-x}S , TiO_2 , and carbon was studied by Fourier transform infrared spectroscopy (FTIR) and the results are given in Figure 3B. The peaks at about 1200 and 1550 cm^{-1} are attributed to the C–C stretching vibration and asymmetric and symmetric stretching band of COO^- , respectively [1,4]. The absorption peaks around 500–700 cm^{-1} for Ti–O vibration represents the interaction of TiO_2 with the carbon [4]. The band at 1030 and 812 cm^{-1} are due to the asymmetric stretching of sulfur functional groups such as S–O [27]. Further, the peaks at 654, 623, and 582 cm^{-1} correspond to the disulfide (S–S) stretching vibrations [27]. It has also been reported in previous studies that the peaks around 1120–1156 cm^{-1} represent the pyrite surface chemistry (Fe=S) and the peaks around 607–622 cm^{-1} represent the stretching S–S and Fe–S bonds [28,29].

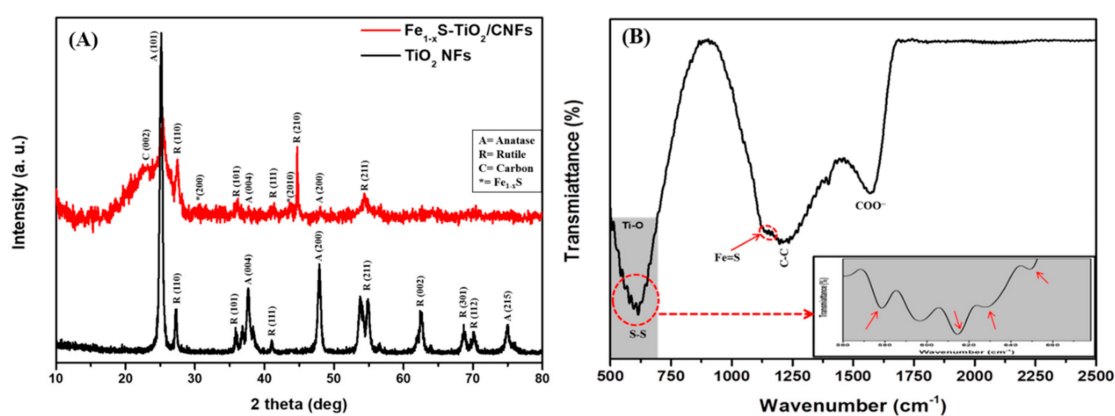


Figure 3. XRD spectra of $\text{Fe}_{1-x}\text{S-TiO}_2/\text{CNFs}$ composite as compared to TiO_2 NFs (A) and FTIR spectra of the $\text{Fe}_{1-x}\text{S-TiO}_2/\text{CNFs}$ composite (B).

The surface composition and chemical state of the samples were further investigated by the X-ray photoelectron spectra (XPS). The survey spectrum indicated signals from Fe, S, Ti, O, and C in the composite sample (Figure 4A). In the high resolution of Fe 2p (Figure 4B), the peaks at ~710.9 and 724.3 eV are attributed to the Fe 2p_{3/2} and Fe 2p_{1/2}, which are in good agreement with the Fe_{1-x}S phase [25]. The peak at 710.9 eV suggests the existence of Fe^{2+} [17]. The high-resolution S 2p (Figure 4C) detected three peaks at ~163.4, 164.1, and 168.7 eV representing the characteristic feature of Fe_{1-x}S [25]. The peaks at ~163.4 and 164.1 eV correspond to S 2p_{3/2} and S 2p_{1/2}, respectively whereas the peak at 168.7 eV corresponds to the S–O bond [17,30]. The high resolution XPS scan of Ti 2p (Figure 4D) showed two peaks at about 458.5 and 464.2 eV, representing the Ti 2p_{3/2} and Ti 2p_{1/2}, respectively [31]. The peak of O 1s (Figure 4E) is centered at ~529.9 eV, which is attributed to the oxide of the titanium [31]. In the XPS spectrum of C 1s (Figure 4F), the peak centered at about 284.21 eV is associated with the C–C [32]. Overall, the obtained results indicated that Fe_{1-x}S and TiO_2 have been introduced into the carbon fiber matrix successfully.

Materials with sufficient porosity and high surface area are considered to enhance electrochemical performance [33,34]. In order to study the specific surface area and the porosity of the synthesized materials, we performed Brunauer–Emmett–Teller (BET) gas sorption analyses (Figure 5A,B). The Nitrogen adsorption–desorption isotherm showed a mesoporous nature of the materials. It was noticed that the BET surface area and total pore volume of $\text{Fe}_{1-x}\text{S-TiO}_2/\text{CNFs}$ composite were higher as compared to TiO_2 NFs whereas the mean pore diameter was found to be lower (Table 1). The interconnected porous structure providing a larger specific surface area in $\text{Fe}_{1-x}\text{S-TiO}_2/\text{CNFs}$ composite

shortens the transport path and establishes a continuous pathway for the electrolyte diffusion [4]. Therefore, we expect a good electrochemical performance from the $\text{Fe}_{1-x}\text{S-TiO}_2/\text{CNFs}$ composite sample.

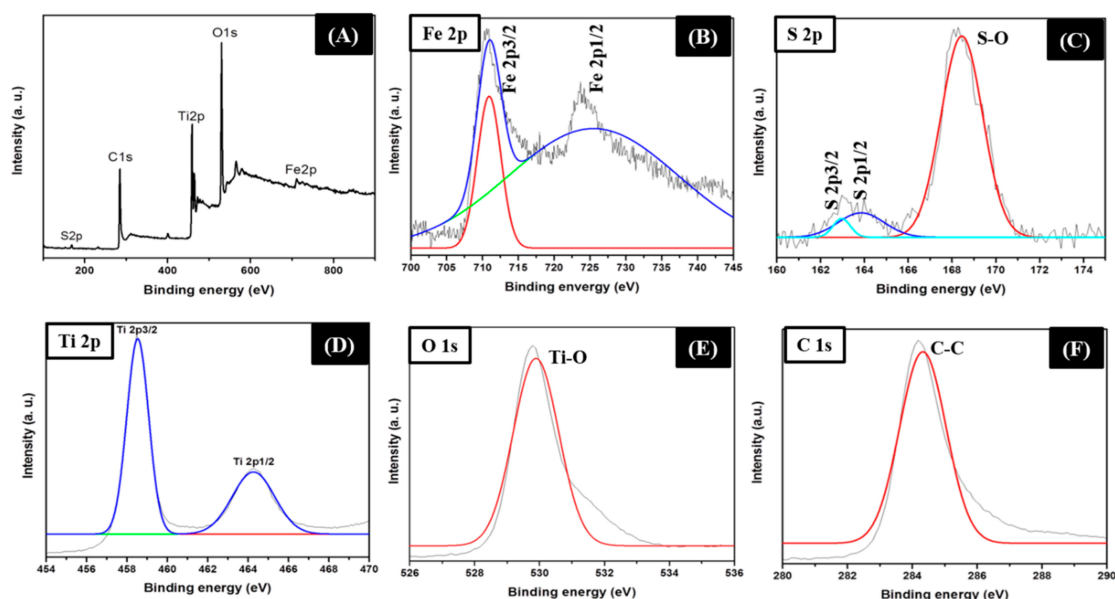


Figure 4. XPS survey (A) and high resolution XPS scan for Fe 2p (B), S 2p (C), Ti 2p (D), O 1s (E), and C 1s (F) of the $\text{Fe}_{1-x}\text{S-TiO}_2/\text{CNFs}$ composite.

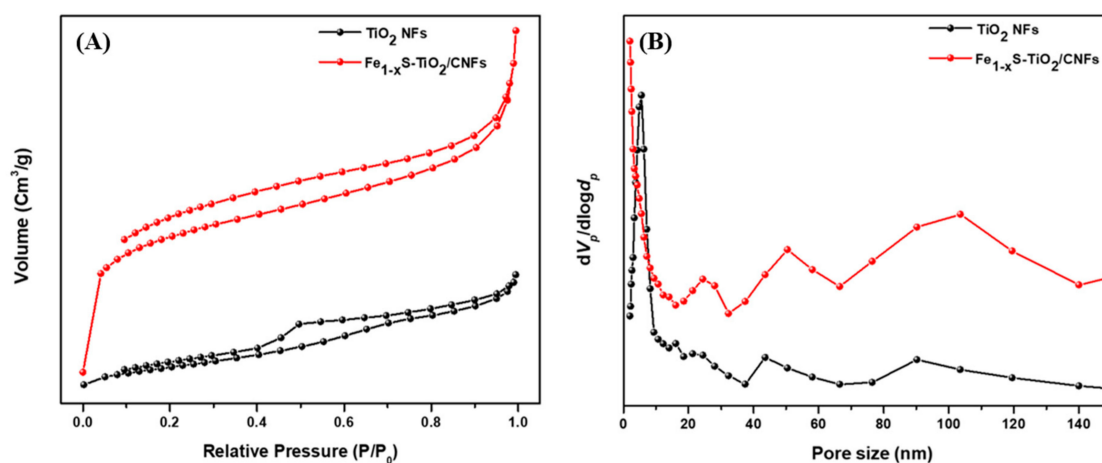


Figure 5. Nitrogen adsorption and desorption isotherm (A) and pore size distribution graph (B) for the $\text{Fe}_{1-x}\text{S-TiO}_2/\text{CNFs}$ composite as compared to TiO_2 NFs.

Table 1. Surface area, pore volume, and pore diameter of the $\text{Fe}_{1-x}\text{S-TiO}_2/\text{CNFs}$ composite as compared to the TiO_2 NFs.

Sample	BET Surface Area (m^2/g)	Total Pore Volume (cm^3/g)	Mean Pore Diameter (nm)
TiO_2 NFs	44.507	0.07209	6.479
$\text{Fe}_{1-x}\text{S-TiO}_2/\text{CNFs}$	291.06	0.2402	3.3007

The cyclic voltammetry curves of the pristine TiO_2 NFs and the composite sample were recorded in a 2 M KOH electrolyte solution in the voltage range of 0 to 0.5 V at various scan rates as shown in Figure 6A,B. The CV profile exhibited a pseudocapacitive nature in both cases; however, there is slight difference in the redox peaks which is due to the structural difference in the two electrodes. Figure 6C shows the comparative CV curves of the pristine TiO_2 NFs and $\text{Fe}_{1-x}\text{S-TiO}_2/\text{CNFs}$ at a

scan rate of 10 mV/s. As in the figure, the area under CV curve of $\text{Fe}_{1-x}\text{S-TiO}_2/\text{CNFs}$ is higher than that of pristine TiO_2 NFs which suggests the higher capacitance of $\text{Fe}_{1-x}\text{S-TiO}_2/\text{CNFs}$ as compared to TiO_2 NFs. The addition of Fe_{1-x}S and carbon in the TiO_2 could have the combined effect of the faradiac capacitance of the Fe_{1-x}S and double-layer capacitance of the carbon, thereby enhancing the electrochemical performance of the composite nanofiber. The specific capacitance of the as-fabricated composite materials was calculated by the GCD method and compared with pristine TiO_2 NFs. The GCD was recorded over the potential window between 0 to 0.45 at the current density of 1, 2, 3, 4, and 5 A/g. It can be noted that the charge-discharge curves are consistent with the CV curves, suggesting a good pseudocapacitive behavior. The increase in the current density led to a decrease in discharge time (Figure 7A,B). The specific capacitances of TiO_2 NFs at the current densities of 1, 2, 3, 4, and 5 were recorded as 44.2, 20.8, 11.3, 7.1, 4.3 F/g, respectively. The specific capacitances for the $\text{Fe}_{1-x}\text{S-TiO}_2/\text{CNFs}$ composite were found to be 138.8, 126.3, 115.2, 100.4, and 95.4 F/g at the current densities of 1, 2, 3, 4, and 5 A/g, respectively (Figure 7C). The specific capacitance is mainly attributed to the porosity and conductivity, which are advantageous properties for the adsorption, penetration, and fast transportation of ions [33]. The cyclic stability is one of the important features of the electrode material in supercapacitor [1]. Therefore, we studied the stability of the $\text{Fe}_{1-x}\text{S-TiO}_2/\text{CNFs}$ composite electrode by the GCD method for 2000 cycles and the results are given in Figure 8A. As in the figure, it can be observed that the capacitance retention is constant up to 100 cycles, whereas after 100 cycles, it is slightly decreased. The decline in capacitance retention pronounced more after 1000 cycles. The electrode material showed about 83% capacitive retention after 2000 cycles, suggesting good stability. The GCD curves showing the stability up to 50 cycles can be seen in the inset of Figure 8A. Next, the EIS were recorded (frequency range: 0.001–10,000 Hz) before and after the stability test to study the electrical conductivity of the electrode material (Figure 8B). As in the figure, after the stability test, the diameter of the semicircle at the high-frequency region is slightly increased as compared to that before the stability test, which suggests a slight reduction in the conductivity of the material [35,36]. Overall, it can be concluded that the as-synthesized $\text{Fe}_{1-x}\text{S-TiO}_2/\text{CNFs}$ composite showed a good electrochemical performance showing some potentiality for the supercapacitor electrode. In order to compare the performance of the $\text{Fe}_{1-x}\text{S-TiO}_2/\text{CNFs}$ electrode with some previously investigated TiO_2 -based electrode, a table is given (Table 2). It can be seen that the performance of the $\text{Fe}_{1-x}\text{S-TiO}_2/\text{CNFs}$ as electrode material for supercapacitor is satisfactory.

Table 2. Comparison of the electrochemical performance of as-synthesized $\text{Fe}_{1-x}\text{S-TiO}_2/\text{CNFs}$ composite as a supercapacitor electrode material with some other TiO_2 -based electrodes.

S.N.	Electrode Material	Fabrication Method	Electrolyte	Specific Capacitance	Stability	Ref.
1	TiO_2 -nanotube-array	Electrochemical anodization	LiPF_6 1.2 M	5.12 mF/cm ² at 100 $\mu\text{A}/\text{cm}^2$	88%	[37]
2	TiO_2 NFs	Electrospinning	Li_2SO_4 1 mol L ⁻¹	75 F/g at 1 mA g ⁻¹	95% after 5000 cycles 78% after 10,000 cycles	[38]
3.	KOH-treated TiO_2 NFs	Electrospinning	Na_2SO_4 1 mol L ⁻¹	65.84 F/g at 1 mV/s	97.8% after 4000 cycles	[39]
4	$\text{TiO}_2@\text{CNF}$	Electrospinning	KOH 6M	151.5 F/g at 1 A/g	84% after 2000 cycles	[40]
5	TiO_2 -CNFs	Electrospinning	KOH 2 M	106.57 F/g at 1 A/g	-	[4]
6	Fe- TiO_2/CNFs	Electrospinning	KOH 1 M	137 F/g at 5 mV/s	-	[41]
7	$\text{Fe}_{1-x}\text{S-TiO}_2/\text{CNFs}$	Electrospinning	KOH 2 M	138 F/g at 1 A/g	83% after 2000 cycles	This study

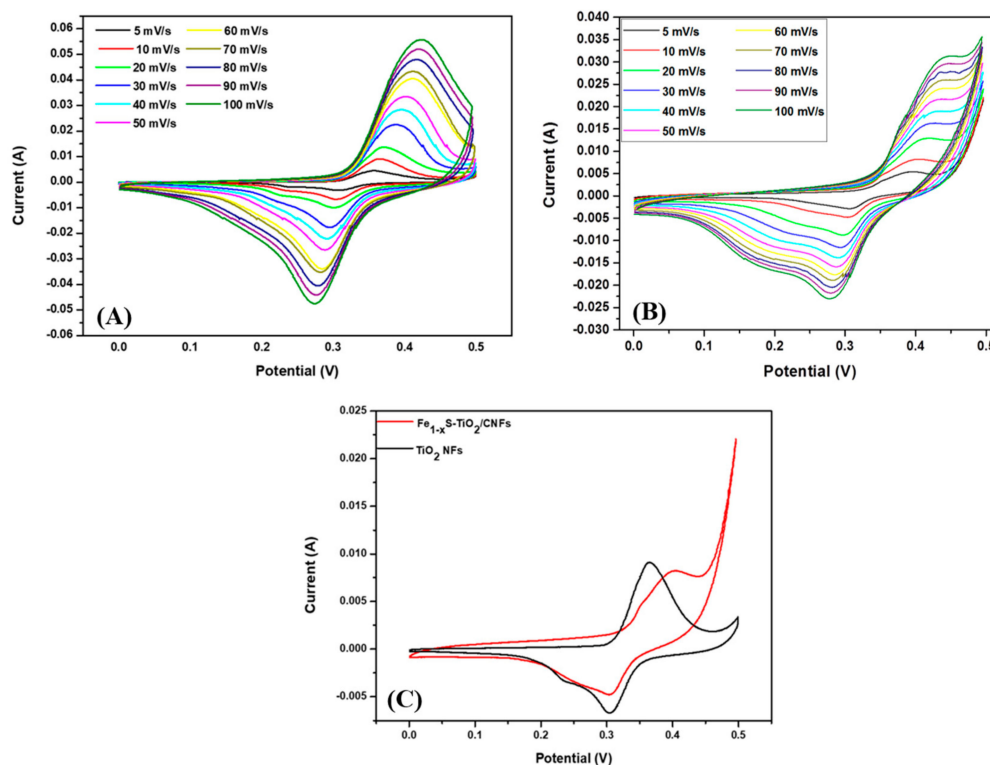


Figure 6. Cyclic voltammetry (CV) curves of TiO_2 NFs (A) and $\text{Fe}_{1-x}\text{S-TiO}_2/\text{CNFs}$ composite electrode (B) at various scan rates. (C) shows the CV results for the TiO_2 NFs and $\text{Fe}_{1-x}\text{S-TiO}_2/\text{CNFs}$ composite electrodes at a 10 mV/s scan rate.

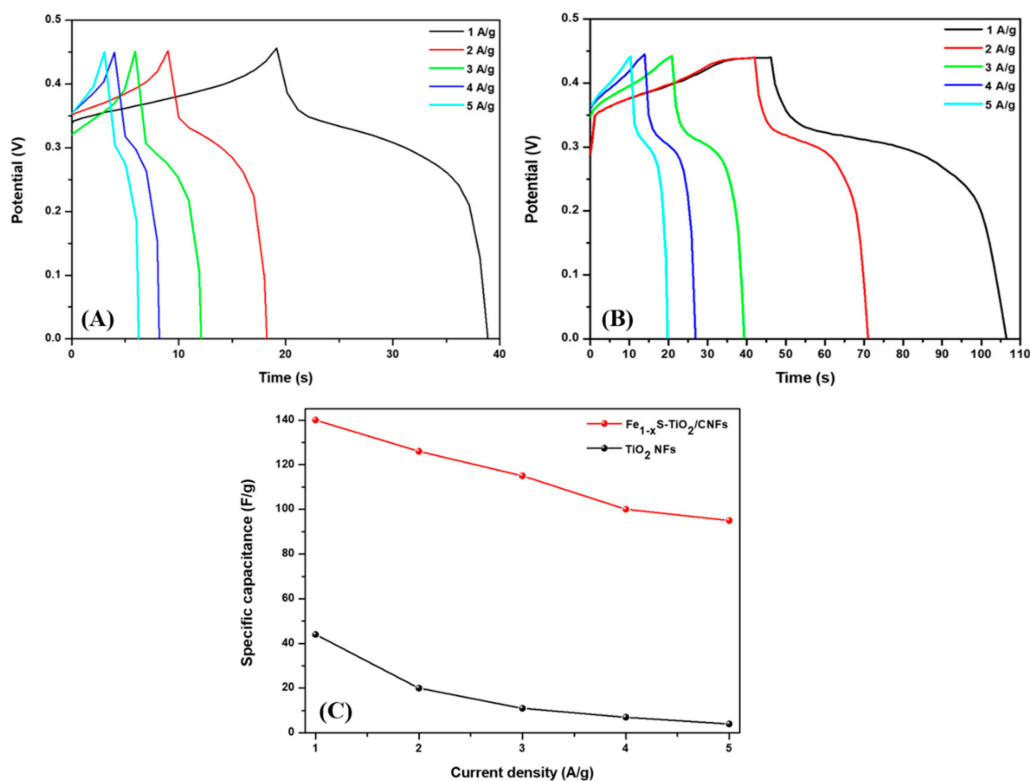


Figure 7. Galvanostatic charge–discharge (GCD) curves of TiO_2 NFs (A) and $\text{Fe}_{1-x}\text{S-TiO}_2/\text{CNFs}$ composite (B). (C) represents the specific capacitance of $\text{Fe}_{1-x}\text{S-TiO}_2/\text{CNFs}$ composite electrode as compared to TiO_2 NFs at various current densities.

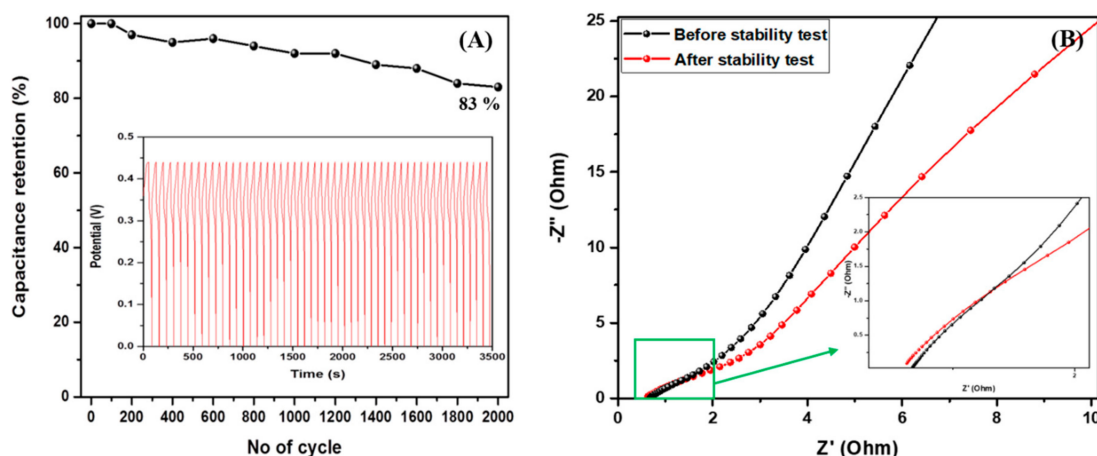


Figure 8. Cyclic stability for 2000 cycles (A) and EIS profile of the $\text{Fe}_{1-x}\text{S-TiO}_2/\text{CNFs}$ composite electrode (B). Inset A represents GCD profiles for 50 cycles.

4. Conclusions

In summary, the $\text{Fe}_{1-x}\text{S-TiO}_2/\text{CNFs}$ composite was prepared by electrospinning followed by the carbonization under the inert atmosphere. The $\text{Fe}_{1-x}\text{S-TiO}_2$ loaded carbon nanofibers possessed high surface area, enough porosity, and good conductivity which provide a fast ion diffusion, thereby boosting electrochemical performances. This study suggested that the integration of Fe_{1-x}S and TiO_2 in the carbon fibers could be a good strategy to enhance the electrochemical behavior of the TiO_2 -based material.

Author Contributions: Conceptualization, B.P.; methodology, B.P.; software, B.P.; validation, M.P. and H.R.P.; formal analysis, B.P.; investigation, B.P.; resources, M.P.; data curation, B.P.; writing—original draft preparation, B.P.; writing—review and editing, B.P.; visualization, B.P.; supervision, M.P.; project administration, M.P.; funding acquisition, M.P. All authors have read and agreed to the published version of the manuscript.

Funding: This research was supported by the Traditional Culture Convergence Research Program through the National Research Foundation of Korea (NRF) funded by the Ministry of Science, ICT & Future Planning (2018M3C1B5052283). This work was also supported by the National Research Foundation of Korea (NRF) grant funded by the Korea government (MSIT) (No. NRF-2019R1A2C1004467).

Conflicts of Interest: The authors declare no conflict of interest.

References

- Pant, B.; Park, M.; Ojha, G.P.; Park, J.; Kuk, Y.-S.; Lee, E.-J.; Kim, H.-Y.; Park, S.-J. Carbon nanofibers wrapped with zinc oxide nano-flakes as promising electrode material for supercapacitors. *J. Colloid Interface Sci.* **2018**, *522*, 40–47. [[CrossRef](#)]
- Lee, D.G.; Kim, B.-H. MnO₂ decorated on electrospun carbon nanofiber/graphene composites as supercapacitor electrode materials. *Synth. Metals* **2016**, *219*, 115–123. [[CrossRef](#)]
- Lin, S.-C.; Lu, Y.-T.; Chien, Y.-A.; Wang, J.-A.; Chen, P.-Y.; Ma, C.-C.M.; Hu, C.-C. Asymmetric supercapacitors based on electrospun carbon nanofiber/sodium-pre-intercalated manganese oxide electrodes with high power and energy densities. *J. Power Sources* **2018**, *393*, 1–10. [[CrossRef](#)]
- Pant, B.; Park, M.; Park, S.-J. TiO₂ NPs Assembled into a Carbon Nanofiber Composite Electrode by a One-Step Electrospinning Process for Supercapacitor Applications. *Polymers* **2019**, *11*, 899. [[CrossRef](#)] [[PubMed](#)]
- Afif, A.; Rahman, S.M.H.; Tasfiah Azad, A.; Zaini, J.; Islan, M.A.; Azad, A.K. Advanced materials and technologies for hybrid supercapacitors for energy storage – A review. *J. Energy Storage* **2019**, *25*, 100852. [[CrossRef](#)]
- Ojha, G.P.; Pant, B.; Park, S.-J.; Park, M.; Kim, H.-Y. Synthesis and characterization of reduced graphene oxide decorated with CeO₂-doped MnO₂ nanorods for supercapacitor applications. *J. Colloid Interface Sci.* **2017**, *494*, 338–344. [[CrossRef](#)] [[PubMed](#)]

7. Ramadoss, A.; Kim, G.-S.; Kim, S.J. Fabrication of reduced graphene oxide/TiO₂ nanorod/reduced graphene oxide hybrid nanostructures as electrode materials for supercapacitor applications. *CrystEngComm* **2013**, *15*, 10222–10229. [[CrossRef](#)]
8. Heng, I.; Lai, C.W.; Juan, J.C.; Numan, A.; Iqbal, J.; Teo, E.Y.L. Low-temperature synthesis of TiO₂ nanocrystals for high performance electrochemical supercapacitors. *Ceramics Int.* **2019**, *45*, 4990–5000. [[CrossRef](#)]
9. Yang, S.; Li, Y.; Sun, J.; Cao, B. Laser induced oxygen-deficient TiO₂/graphene hybrid for high-performance supercapacitor. *J. Power Sources* **2019**, *431*, 220–225. [[CrossRef](#)]
10. Hsieh, C.-T.; Chang, C.-C.; Chen, W.-Y.; Hung, W.-M. Electrochemical capacitance from carbon nanotubes decorated with titanium dioxide nanoparticles in acid electrolyte. *J. Phys. Chem. Solids* **2009**, *70*, 916–921. [[CrossRef](#)]
11. Verma, S.; Sinha-Ray, S.; Sinha-Ray, S. Electrospun CNF Supported Ceramics as Electrochemical Catalysts for Water Splitting and Fuel Cell: A Review. *Polymers* **2020**, *12*, 238. [[CrossRef](#)] [[PubMed](#)]
12. Liu, Y.; Zeng, Z.; Bloom, B.; Waldeck, D.H.; Wei, J. Stable Low-Current Electrodeposition of α -MnO₂ on Superaligned Electrospun Carbon Nanofibers for High-Performance Energy Storage. *Small* **2018**, *14*, 1703237. [[CrossRef](#)] [[PubMed](#)]
13. Ikkurthi, K.D.; Srinivasa Rao, S.; Jagadeesh, M.; Reddy, A.E.; Anitha, T.; Kim, H.-J. Synthesis of nanostructured metal sulfides via a hydrothermal method and their use as an electrode material for supercapacitors. *New J. Chem.* **2018**, *42*, 19183–19192. [[CrossRef](#)]
14. Rui, X.; Tan, H.; Yan, Q. Nanostructured metal sulfides for energy storage. *Nanoscale* **2014**, *6*, 9889–9924. [[CrossRef](#)]
15. Chen, Y.; Xu, S.; Li, Y.; Jacob, R.J.; Kuang, Y.; Liu, B.; Wang, Y.; Pastel, G.; Salamanca-Riba, L.G.; Zachariah, M.R.; et al. FeS₂ Nanoparticles Embedded in Reduced Graphene Oxide toward Robust, High-Performance Electrocatalysts. *Adv. Energy Mater.* **2017**, *7*, 1700482. [[CrossRef](#)]
16. Karade, S.S.; Dwivedi, P.; Majumder, S.; Pandit, B.; Sankapal, B.R. First report on a FeS-based 2 V operating flexible solid-state symmetric supercapacitor device. *Sustainable Energy Fuels* **2017**, *1*, 1366–1375. [[CrossRef](#)]
17. Liu, X.; Yang, Q.; Mi, M.; Kong, W.; Ge, Y.; Ma, J.; Hu, J. Fe_{1-x}S/reduced graphene oxide composite as anode material for aqueous rechargeable Ni/Fe batteries. *J. Alloys Comp.* **2019**, *800*, 99–106. [[CrossRef](#)]
18. Liu, Y.; Fang, Y.; Zhao, Z.; Yuan, C.; Lou, X.W. A Ternary Fe_{1-x}S@Porous Carbon Nanowires/Reduced Graphene Oxide Hybrid Film Electrode with Superior Volumetric and Gravimetric Capacities for Flexible Sodium Ion Batteries. *Adv. Energy Mater.* **2019**, *9*, 1803052. [[CrossRef](#)]
19. Zhu, Y.; Fan, X.; Suo, L.; Luo, C.; Gao, T.; Wang, C. Electrospun FeS₂@Carbon Fiber Electrode as a High Energy Density Cathode for Rechargeable Lithium Batteries. *ACS Nano* **2016**, *10*, 1529–1538. [[CrossRef](#)] [[PubMed](#)]
20. Pant, B.; Pant, H.R.; Park, M.; Liu, Y.; Choi, J.-W.; Barakat, N.A.M.; Kim, H.-Y. Electrospun CdS–TiO₂ doped carbon nanofibers for visible-light-induced photocatalytic hydrolysis of ammonia borane. *Cata. Commun.* **2014**, *50*, 63–68. [[CrossRef](#)]
21. Wetchakun, N.; Incessungvorn, B.; Wetchakun, K.; Phanichphant, S. Influence of calcination temperature on anatase to rutile phase transformation in TiO₂ nanoparticles synthesized by the modified sol–gel method. *Mater. Lett.* **2012**, *82*, 195–198. [[CrossRef](#)]
22. Wang, H.; Huang, X.; Li, W.; Gao, J.; Xue, H.; Li, R.K.Y.; Mai, Y.-W. TiO₂ nanoparticle decorated carbon nanofibers for removal of organic dyes. *Colloids Sur. A Physicochem. Eng. Aspects* **2018**, *549*, 205–211. [[CrossRef](#)]
23. Pant, B.; Barakat, N.A.M.; Pant, H.R.; Park, M.; Saud, P.S.; Kim, J.-W.; Kim, H.-Y. Synthesis and photocatalytic activities of CdS/TiO₂ nanoparticles supported on carbon nanofibers for high efficient adsorption and simultaneous decomposition of organic dyes. *J. Colloid Interface Sci.* **2014**, *434*, 159–166. [[CrossRef](#)] [[PubMed](#)]
24. Pant, B.; Pant, H.R.; Barakat, N.A.M.; Park, M.; Jeon, K.; Choi, Y.; Kim, H.-Y. Carbon nanofibers decorated with binary semiconductor (TiO₂/ZnO) nanocomposites for the effective removal of organic pollutants and the enhancement of antibacterial activities. *Ceramics Int.* **2013**, *39*, 7029–7035. [[CrossRef](#)]
25. Wang, C.; Lan, M.; Zhang, Y.; Bian, H.; Yuen, M.-F.; Ostrikov, K.; Jiang, J.; Zhang, W.; Li, Y.Y.; Lu, J. Fe_{1-x}S/C nanocomposites from sugarcane waste-derived microporous carbon for high-performance lithium ion batteries. *Green Chem.* **2016**, *18*, 3029–3039. [[CrossRef](#)]

26. Argueta-Figueroa, L.; Torres-Gómez, N.; García-Contreras, R.; Vilchis-Nestor, A.R.; Martínez-Alvarez, O.; Acosta-Torres, L.S.; Arenas-Arrocena, M.C. Hydrothermal synthesis of pyrrhotite (Fex-1S) nanoplates and their antibacterial, cytotoxic activity study. *Pro. Natural Sci. Mater. Int.* **2018**, *28*, 447–455. [[CrossRef](#)]
27. Venkateshalu, S.; Goban Kumar, P.; Kollu, P.; Jeong, S.K.; Grace, A.N. Solvothermal synthesis and electrochemical properties of phase pure pyrite FeS₂ for supercapacitor applications. *Electrochimica Acta* **2018**, *290*, 378–389. [[CrossRef](#)]
28. Khabbaz, M.; Entezari, M.H. Simple and versatile one-step synthesis of FeS₂ nanoparticles by ultrasonic irradiation. *J. Colloid Interface Sci.* **2016**, *470*, 204–210. [[CrossRef](#)]
29. Middy, S.; Layek, A.; Dey, A.; Ray, P.P. Synthesis of Nanocrystalline FeS₂ with Increased Band Gap for Solar Energy Harvesting. *J. Mater. Sci. Tech.* **2014**, *30*, 770–775. [[CrossRef](#)]
30. Wang, M.-H.; Xue, H.-G.; Guo, S.-P. In situ hydrothermal synthesis of rGO-wrapped Fe_{1-x}S particles for lithium storage. *J. Mater. Res.* **2019**, *34*, 3186–3194. [[CrossRef](#)]
31. Wang, X.; Xiang, Q.; Liu, B.; Wang, L.; Luo, T.; Chen, D.; Shen, G. TiO₂ modified FeS Nanostructures with Enhanced Electrochemical Performance for Lithium-Ion Batteries. *Sci. Reports* **2013**, *3*, 2007. [[CrossRef](#)] [[PubMed](#)]
32. Liu, Y.; Zhong, W.; Yang, C.; Pan, Q.; Li, Y.; Wang, G.; Zheng, F.; Xiong, X.; Liu, M.; Zhang, Q. Direct synthesis of FeS/N-doped carbon composite for high-performance sodium-ion batteries. *J. Mater. Chem. A* **2018**, *6*, 24702–24708. [[CrossRef](#)]
33. Daubert, J.S.; Lewis, N.P.; Gotsch, H.N.; Mundy, J.Z.; Monroe, D.N.; Dickey, E.C.; Losego, M.D.; Parsons, G.N. Effect of Meso- and Micro-Porosity in Carbon Electrodes on Atomic Layer Deposition of Pseudocapacitive V₂O₅ for High Performance Supercapacitors. *Chem. Mater.* **2015**, *27*, 6524–6534. [[CrossRef](#)]
34. Zhi, M.; Liu, S.; Hong, Z.; Wu, N. Electrospun activated carbon nanofibers for supercapacitor electrodes. *RSC Advances* **2014**, *4*, 43619–43623. [[CrossRef](#)]
35. Pant, B.; Park, M.; Park, S.-J. MoS₂/CdS/TiO₂ ternary composite incorporated into carbon nanofibers for the removal of organic pollutants from water. *Inorg. Chem. Commun.* **2019**, *102*, 113–119. [[CrossRef](#)]
36. Pant, B.; Ojha, G.P.; Kim, H.-Y.; Park, M.; Park, S.-J. Fly-ash-incorporated electrospun zinc oxide nanofibers: Potential material for environmental remediation. *Environmental Pollution* **2019**, *245*, 163–172. [[CrossRef](#)]
37. Ahmed, F.; Pervez, S.A.; Aljaafari, A.; Alshoabi, A.; Abuhimd, H.; Oh, J.; Koo, B.H. Fabrication of TiO₂-Nanotube-Array-Based Supercapacitors. *Micromachines* **2019**, *10*, 742. [[CrossRef](#)]
38. Kuchi, C.; Narayana, A.L.; Hussain, O.M.; Reddy, P.S. Electrospun TiO₂ nanofiber electrodes for high performance supercapacitors. *Mater. Res. Express* **2020**, *7*, 015098. [[CrossRef](#)]
39. He, X.; Yang, C.P.; Zhang, G.L.; Shi, D.W.; Huang, Q.A.; Xiao, H.B.; Liu, Y.; Xiong, R. Supercapacitor of TiO₂ nanofibers by electrospinning and KOH treatment. *Mater. Des.* **2016**, *106*, 74–80. [[CrossRef](#)]
40. Tang, K.; Li, Y.; Cao, H.; Su, C.; Zhang, Z.; Zhang, Y. Amorphous-crystalline TiO₂/carbon nanofibers composite electrode by one-step electrospinning for symmetric supercapacitor. *Electrochimica Acta* **2016**, *190*, 678–688. [[CrossRef](#)]
41. Tolba, G.; Motlak, M.; Bastaweesy, A.M.; Ashour, E.A.; Abdelmoez, W.; El-Newehy, M.; Barakat, N. Synthesis of Novel Fe-doped Amorphous TiO₂/C Nanofibers for Supercapacitors Applications. *Int. J. Electrochem. Sci.* **2015**, *10*, 3117–3123.

Sample Availability: Samples of the compounds are not available from the authors.



© 2020 by the authors. Licensee MDPI, Basel, Switzerland. This article is an open access article distributed under the terms and conditions of the Creative Commons Attribution (CC BY) license (<http://creativecommons.org/licenses/by/4.0/>).